Key Points:
- High wave speeds in the forearc crust of Cascadia help explain the absent Moho that is commonly ascribed to mantle hydration
- Lower-crustal magma storage appears offset from the Mount St. Helens edifice, which is offset west of the main arc line
- Crustal structure plays a critical role in the location of volcanism and helps explain the unusual trenchward location of Mount St. Helens

Shear Velocity Structure From Ambient Noise and Teleseismic Surface Wave Tomography in the Cascades Around Mount St. Helens

Kayla J. Crosbie[1], Geoffrey A. Abers[1] , Michael Everett Mann[1] , Helen A. Janiszewski[2] , Kenneth C. Creager[3] , Carl W. Ulberg[3] , and Seth C. Moran[4]

[1]Department of Earth and Atmospheric Sciences, Cornell University, Ithaca, NY, USA, [2]Department of Terrestrial Magnetism, Carnegie Institution for Science, Washington, DC, USA, [3]Department of Earth and Space Sciences, University of Washington, Seattle, WA, USA, [4]U.S. Geological Survey Cascades Volcano Observatory, Vancouver, WA, USA

Abstract Mount St. Helens (MSH) lies in the forearc of the Cascades where conditions should be too cold for volcanism. To better understand thermal conditions and magma pathways beneath MSH, data from a dense broadband array are used to produce high-resolution tomographic images of the crust and upper mantle. Rayleigh-wave phase-velocity maps and three-dimensional images of shear velocity (Vs), generated from ambient noise and earthquake surface waves, show that west of MSH the middle-lower crust is anomalously fast (3.95 ± 0.1 km/s), overlying an anomalously slow uppermost mantle (4.0–4.2 km/s). This combination renders the forearc Moho weak to invisible, with crustal velocity variations being a primary cause; fast crust is necessary to explain the absent Moho. Comparison with predicted rock velocities indicates that the fast crust likely consists of gabbros and basalts of the Siletzia terrane, an accreted oceanic plateau. East of MSH where magmatism is abundant, middle-lower crust Vs is low (3.45–3.6 km/s), consistent with hot and potentially partly molten crust of more intermediate to felsic composition. This crust overlies mantle with more typical wave speeds, producing a strong Moho. The sharp boundary in crust and mantle Vs within a few kilometers of the MSH edifice correlates with a sharp boundary from low heat flow in the forearc to high arc heat flow and demonstrates that the crustal terrane boundary here couples with thermal structure to focus lateral melt transport from the lower crust westward to arc volcanoes.

1. Introduction

Subduction-related volcanism typically occurs where the top of the subducting plate reaches about 100-km depth, defining a sharp volcanic front (Syracuse & Abers, 2006). In the mantle wedge, a sharp boundary 25–50 km trenchward of the arc separates cold forearc from hot, flowing subarc and backarc mantle; both heat flow and seismic attenuation delineate this boundary (e.g., Syracuse et al., 2010; Wada & Wang, 2009). The volcanic arc itself is typically associated with locally high heat flow, perhaps due to advective transport by melt (Rees Jones et al., 2018), indicating a complex feedback between conductive cooling, wedge flow, and magma transport. This transition from hot subarc mantle to cold forearc mantle has been suggested to allow substantial hydration of the forearc mantle wedge (e.g., Hyndman & Peacock, 2003), a hypothesis supported by an absent Moho in the Cascadia forearc (Bostock et al., 2002; Brocher et al., 2003; Hansen et al., 2016).

However, the location of surface volcanism relative to the slab sometimes deviates from this pattern, suggesting other controls may be also important. One obvious anomaly is Mount St. Helens (MSH), which sits significantly trenchward of the Cascade volcanic arc (Figure 1). Volcanism in the Cascades typically occurs where the top of the subducting Juan de Fuca plate reaches 80- to 90-km depth (McCrory et al., 2012). MSH, the most active Holocene volcano in the Cascades, lies 35–50 km west of this arc front as do abundant vents farther south (Figure 2). The melt transport pathway is not understood, since heat flow within a few kilometers of the MSH edifice is markedly low compared to the arc and backarc (Blackwell et al., 1990; van Keken et al., 2018). Furthermore, erupted dacites record equilibration temperatures of 925–940 °C at lower crustal pressures of 700–900 MPa (Blatter et al., 2017), but such high temperatures seem inconsistent with low heat flow and the inferred presence of serpentinized mantle. Nearby basaltic vents require even hotter mantle temperatures (Leeman et al., 2005). Hence, lateral transport of magma to MSH
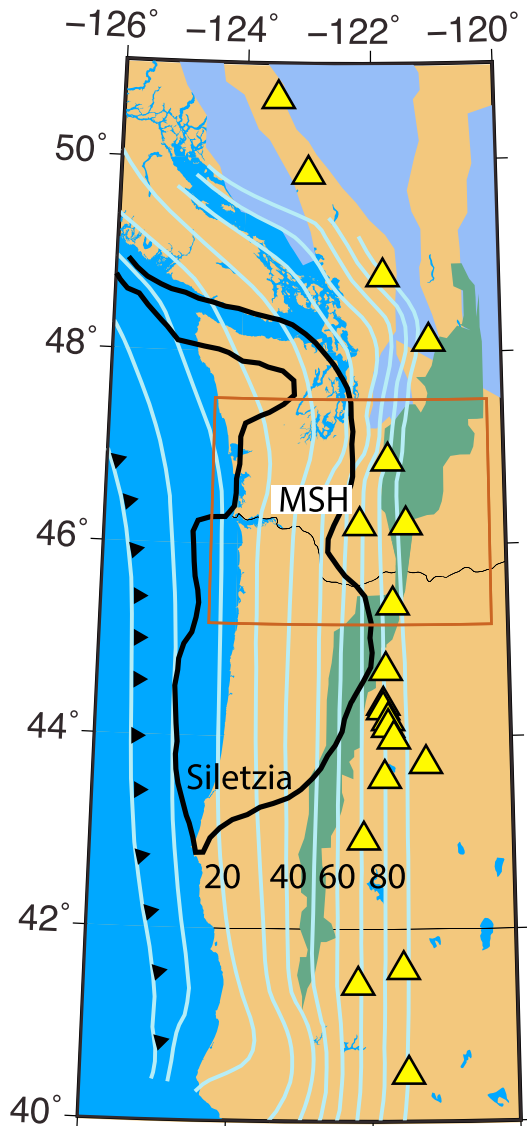
Figure 1. Regional setting of the Cascades. Black outline: Siletzia terrane (Wells et al., 2014); green field: Tertiary Cascades arc volcanics; blue field: exposed North American basement (Reed et al., 2004); blue lines: top of subducting slab (McCrory et al., 2012); yellow triangles: main arc volcanoes (Hildreth, 2007). Brown box is location for Figure 2. MSH = Mount St. Helens.

from the east seems likely, as inferred from recent MT and seismic images (Bedrosian et al., 2018; Hansen et al., 2016; Kiser et al., 2016).

To better understand this anomaly and the location of arc volcanoes in general, we use the imaging Magma Under St. Helens (iMUSH) broadband seismic array to image crustal and upper mantle structure. The iMUSH broadband array (e.g., Mann et al., 2019) has 70 seismometers spaced every 10 km within 50 km of the MSH edifice, providing the highest-resolution three-dimensional (3-D) images of deep structure beneath MSH, and perhaps any arc volcano, to date. The broadband array complements iMUSH active-source seismic and magnetotelluric imaging (Bedrosian et al., 2018; Kiser et al., 2016). Here, we measure Rayleigh wave phase velocities from ambient noise and integrate those observations with earthquake-based surface-wave phase velocities from a parallel study (Janiszewski et al., 2019). Phase-velocity maps from both methods are inverted for shear velocity (Vs) throughout the crust and uppermost mantle. The resulting images reveal a clear correlation between the location of volcanic vents and preexisting crustal structure; in particular, the eastern boundary of the mafic Siletzia terrane in the Cascadia forearc (Wells et al., 2014) may control volcano location. This terrane has anomalously high Vs in the lower crust, which could explain the absence of a forearc Moho in Cascadia particularly when combined with low Vs in the underlying hydrated forearc mantle. Low shear-wave velocities in the middle and lower crust between MSH, Mount Adams, Mount Rainier, and Indian Heaven support the presence of partial melt there, potentially indicating a laterally displaced melt source for MSH.

2. Tectonic Overview

Volcanism in the Cascades is a product of the Juan de Fuca Plate subducting beneath North America. This subduction zone is one of the warmest globally (Hyndman & Wang, 1993; Syracuse et al., 2010), with the spreading ridge less than 250 km from the volcanic arc. One consequence is that the slab can substantially dehydrate at shallow depths and can produce a fully hydrated forearc in the subcontinental mantle (Abers et al., 2017). Since hydrated mantle (serpentinite) has much lower wave speeds than typical peridotite, a hydrated mantle should significantly reduce the wave speeds across the Moho, potentially explaining the observed absence of the Moho in the Cascadia forearc (Bostock et al., 2002; Brocher et al., 2003).

Heat flow is significantly lower in the Cascadia forearc than immediately east of MSH (34 ± 4 mW/m^2 compared to 62 ± 14 mW/m^2 to the east; see the supporting information), indicating lower temperatures in the forearc mantle that allow for the stability of serpentinite (Wada & Wang, 2009). As a result, a weak-to-absent Moho may indicate low temperatures in the uppermost mantle. However, recent laboratory measurements show that antigorite-dominated serpentinite is too fast to reduce seismic wave speeds from mantle to crustal values (Reynard, 2013), and antigorite is the likely serpentine species in the forearc, so other explanations for the absent Moho may be needed.

In the Oregon and Washington forearc, much of the exposed basement (Figure 2) consists of submarine basalts and gabbros of the Siletzia terrane, an oceanic plateau that collided with North America in the Eocene (Wells et al., 2014). The basement east of Siletzia is an amalgam of older terranes of variable affinities (Coney et al., 1980), including mélange belts and roots of continental arcs with generally intermediate to felsic compositions (e.g., Valley et al., 2003). Contacts between Siletzia and these inboard terranes are partly buried by Eocene Puget Group sediments and Eocene-to-present Cascades volcanic and plutonic rocks (Sisson et al., 2014). As a result, the eastern boundary of Siletzia is not observed geologically; its crust is
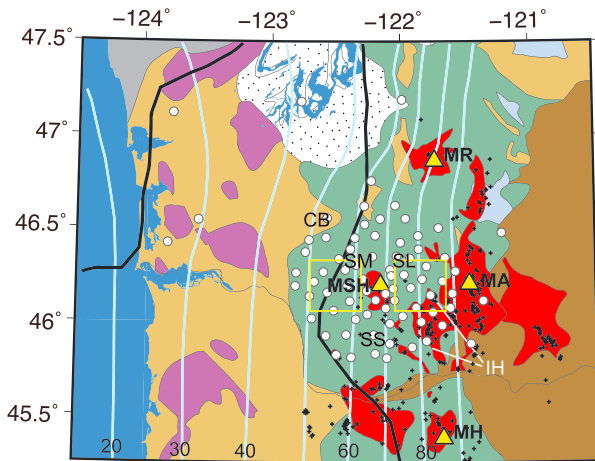
Figure 2. Cascadia near Mount St. Helens (MSH), Mount Adams (MA), Mount Rainier (MR), and Mount Hood (MH; yellow triangles; Hildreth, 2007). White circles: seismic stations used in this study; black crosses: Quaternary vents (Hildreth, 2007); black line: outline of Siletzia (Wells et al., 2014); light blue lines: contours of subducting slab labeled in kilometers (McCrory et al., 2012); yellow boxes: areas of *Vs* averages in Figures 12a and 12b. Solid fields show simplified geology from Sisson et al. (2014): (green) Tertiary volcanics, (tan) Eocene sandstones and silts, (purple) Siletz basalts and gabbros, (brown) Columbia River flood basalts, (red) Quaternary volcanics, (light blue) pre-Cenozoic basement, (stippled white) Puget lowland. Other labeled features: Chehalis Basin (CB), Spud Mountain (SM) pluton, Spirit Lake (SL) pluton, and Silver Star (SS) pluton; Indian Heaven (IH) volcanic field.

Figure 3. Example of phase velocity measurement for the station pair MC08-MO06 (labeled in inset), with interstation distance of 71.6 km. (a) Real part of the Fourier transform of the correlogram. Blue shows the observed correlogram, and purple shows the best fit using the regression method described in the text and in Jin et al. (2015). (b) Corresponding phase velocity estimate. Red dashed line shows the reference starting model, and solid line shows the best fit phase velocities corresponding to purple line in (a). Dots show best fit phase velocity at the frequencies actually parameterized.

thought to terminate just west of MSH based on magnetic anomalies (Wells et al., 2014), although mantle tomography indicates that Siletzia mantle lithosphere may continue to eastern Washington (Schmandt & Humphreys, 2011). The magnetic anomaly pattern can be alternatively modeled as the eastern limit of the serpentinized mantle wedge (Blakely et al., 2005), so the relationship between Siletzia crust and the arc remains uncertain.

Near MSH, several local tomography studies have imaged an upper-crustal magma chamber at 5- to 8-km depth with limited resolution in the lower crust (Lees & Crosson, 1989; Waite & Moran, 2009; De Siena et al., 2014; Kiser et al., 2018). Wang et al. (2017) used ambient noise methodologies to image low velocities in the upper 6 km near the MSH edifice, using a small-aperture high-frequency Nodal array concentrated within 15 km of the MSH summit. Regional studies give hints of a region of partial melt in southwestern Washington between MSH, Mount Adams, and Mount Rainier from active-source seismology (Kiser et al., 2016), magnetotelluric imaging (Bedrosian et al., 2018; Hill et al., 2009), and regional ambient noise tomography (Flinders & Shen, 2017). Although the locations and shapes of the low-velocity/high-conductivity anomalies vary between studies, most indicate an anomalous region of lower crust east of MSH.

3. Data and Methods

3.1. Data

We analyze 12 months of broadband data from the 70 iMUSH broadband instruments and 13 additional broadband stations located within 100 km of MSH from permanent or temporary arrays (Figure 2). This study uses vertical-component signals recorded by a continuous one-sample-per-second data stream or decimated to this sample rate. These data provide structural information from ambient noise at frequencies of 0.05–0.2 Hz. Phase-velocity data at the lower frequencies (0.02–0.05 Hz) are taken from Janiszewski et al. (2019), as discussed below.
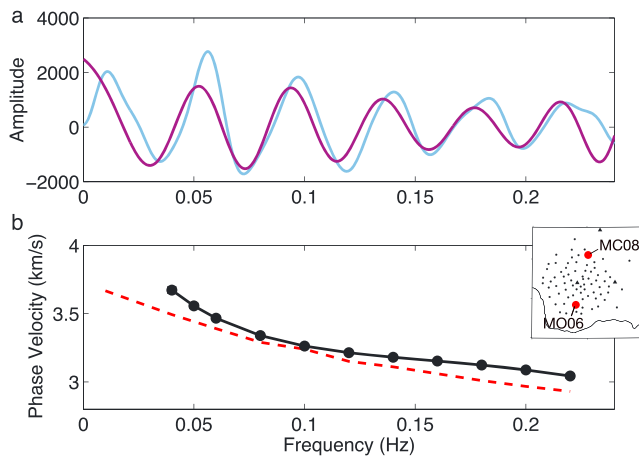
3.2. Measuring Phase Velocities

3.2.1. Phase Velocity From Ambient Noise

Ambient noise is cross-correlated between seismic station pairs to extract the wavefield traveling between the two stations (Aki, 1957; Shapiro & Campillo, 2004), producing a signal dominated by the fundamental-mode Rayleigh wave. Raw seismic traces are preprocessed using a methodology similar to Bensen et al. (2007) and Calkins et al. (2011), to produce 600-s correlograms (cross-correlation records) for each station pair. Phase velocities are calculated from the correlograms in the frequency domain (Ekström et al., 2009), using a modified form of the fitting procedure described by Jin et al. (2015). The real part of the Fourier spectrum of the cross-correlation is fit to a smoothly varying phase velocity $c(\omega)$ at angular frequency ω, with $c(\omega)$ parameterized as a cubic spline with knots every 0.02 Hz from 0.02 to 0.2 Hz. Extra knots are added at 0.01 Hz for a long-period stability and 0.05 Hz where earthquake data also can be used (Figure 3). The fitting procedure simultaneously fits the observed spectrum, minimizes the curvature of the dispersion curve, and enforces a negative slope $dc(\omega)/d\omega$. Although we fit frequencies <0.04 Hz to improve numerical stability, the short interstation distances relative to wavelength are unable to resolve spatial variations at those low frequencies, so they are not analyzed.
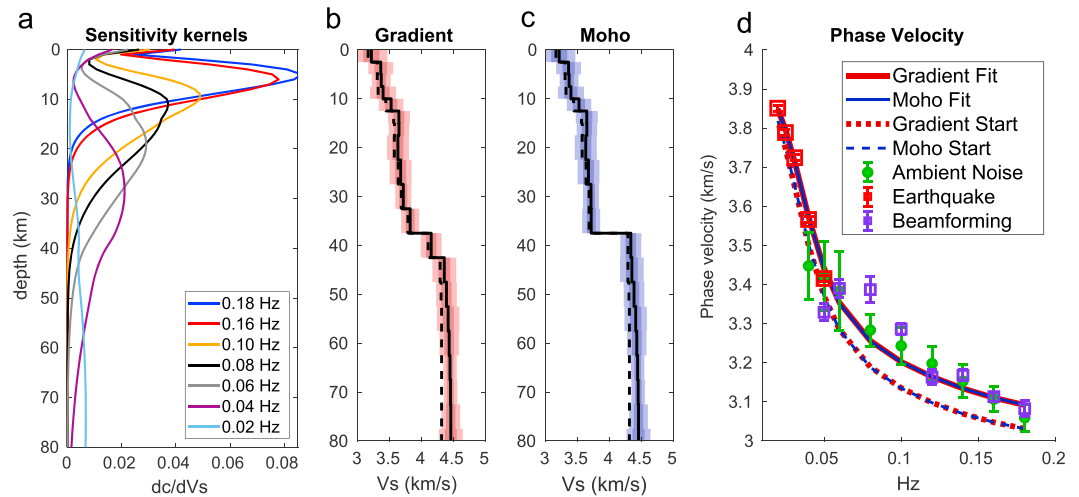
Figure 4. Array-averaged Vs_R and corresponding average dispersion curve $c_R(\omega)$. (a) Sensitivity kernels, showing sensitivity of fundamental-mode Rayleigh phase velocity to Vs variation with depth, at each frequency, calculated from the gradient starting model (Table S1). (b) The gradient model or Vs_R for a smoothed Moho. The original starting model (dashed black) is a moving average of the Group 1 average Vs from Obrebski et al. (2015). Solid black line is the resulting Vs_R, referred to as the "gradient model." Monte Carlo uncertainties shown in solid red, as 1-σ (dark) and 2-σ (light) uncertainties. (c) The Moho Vs_R model and uncertainties with a discontinuity at 37.5-km depth; format same as panel (b). (d) Array-average phase velocity measurements compared with predictions $c_R(\omega)$ for both array-averaged models (solid lines; see legend). Red symbols: phase velocities from earthquake-based surface waves (Janiszewski et al., 2019); green symbols: ambient noise array average; purple symbols: average velocities from the beamforming (see the supporting information). Dashed lines are the predicted dispersion curves for the starting models corresponding to dashed lines in panels (b) and (c).

For the small array here, the phase velocity method offers several advantages to group velocity approaches. First, phase velocity kernels have somewhat greater depth sensitivity than group velocity, and measurements are less affected by amplitude distortion (Yao et al., 2006). Second, as discussed by Calkins et al. (2011), phase velocity measurements for station spacing as small as one cycle (distance/wavelength) provide usable results—the theoretical limit is smaller (Aki, 1957), but in practice low-frequency noise renders even small phase errors problematic at <1 wavelength. This approach is a substantial improvement over typical time domain group-velocity methods, which cannot be used at distances less than three cycles (Bensen et al., 2007). For the short paths analyzed here, a substantial part of the data set lies between one and three wavelengths.

After these and other quality-control measures described in the supporting information, the 83 stations provide between 758 and 2,356 useable station-pair estimates of $c(\omega)$ at each ω (Table S2), with generally more useable pairs for higher ω. Further details are discussed in Crosbie (2018).

3.2.2. Earthquake Surface Wave Phase Velocities

We incorporate measurements of fundamental-mode Rayleigh-wave velocity for frequencies 0.02–0.05 Hz from earthquake sources from a separate study (Janiszewski et al., 2019). These phase-velocity maps are calculated via Helmholtz-equation inversion from Rayleigh waves, sampled by arrays of stations to account for focusing effects (Accardo et al., 2017; Jin & Gaherty, 2015; Lin & Ritzwoller, 2011). Uncertainties for these measurements are calculated from the standard deviations of all individual earthquake phase-velocity maps at each node. At 0.05 Hz, $c(\omega)$ from both ambient noise and earthquake signals is combined in a manner that emphasizes the ambient noise measurements within the array (see the supporting information).

3.3. Network-Averaged Phase Velocities and Shear-Wave Velocities

We first determine a network-averaged reference dispersion curve, $c_R(\omega)$, as a starting model for subsequent spatially varying inversions (Figure 4; Table S2). At frequencies >0.05 Hz the interstation ambient noise phase velocities are averaged over all station pairs, while at <0.05 Hz the earthquake-derived phase velocity maps are spatially averaged in the region where ambient noise tomography has ray coverage. At 0.05 Hz,

both data types are equally weighted. Additionally, $c_R(\omega)$ is validated through independent estimates made by beamforming (supporting information and Figure 4c; following Harmon et al., 2008). At low frequencies the beamforming estimates show more scatter, probably due to difficulty in identifying peaks in beams at low frequencies (Figure S2b).

The reference dispersion curve $c_R(\omega)$ is then inverted to produce a reference shear-velocity (Vs) model with depth z, $Vs_R(z)$ (Figure 4; Table S1) using an iterative nonlinear one-dimensional (1-D) inversion method (Herrmann, 2013). A smoothed $Vs(z)$ model from a nearby study (Group 1 average of Obrebski et al., 2015) is used as the starting model (dashed black line in Figure 4b), with layer thicknesses increasing from 2.5 to 5 km with depth (Table S1). This inversion imposes a first-derivative smoothing constraint on $Vs_R(z)$. Every few iterations the damping value is decreased up to a total factor of 20, with initial damping values comparable to the largest singular value of the design matrix. The result from this inversion is referred to as the "gradient model" (Figure 4b), since Vs varies smoothly with z with no discontinuities. Throughout the text we compare inversions using this gradient model with a 1-D model in which a discontinuity is allowed at 37.5-km depth across which smoothing constraints are removed, referred to as the "Moho model" (Figure 4c). This discontinuity depth corresponds with the model layer boundary closest to the Moho identified in receiver functions (Mann et al., 2019). In inverting for the Moho model, the initial discontinuity is set to 0.6 km/s by perturbing the same starting model (dashed line Figure 4c), but the step is free to change in the inversion.

Uncertainties are evaluated through Monte Carlo simulations in which 100 inversions as described above are repeated, randomly perturbing the starting model $\pm10\%$ at seven reference depths and interpolating between those perturbations (Figures 4b and 4c). The reported uncertainty is based on standard deviations of the 100 models after removing solutions with an error exceeding 20% of the median or greater than a Vs perturbation of 0.3 km/s.

3.4. Phase Velocity Maps From Ambient Noise

At each frequency, the station-pair observations of phase velocity are inverted for two-dimensional (2-D) maps of phase velocity (Figure 5). This 2-D tomographic inversion, detailed in the supporting information and summarized here, solves for spatial perturbations to phase slowness, $1/c(\omega)$, relative to the network-averaged starting value at nodes every 5 km $\times$ 5 km. Station-pair measurements are treated as travel times (distance/c) to approximately linearize the inversions. These inversions use finite frequency kernels (Lin & Ritzwoller, 2010) to relate path-averaged measurements to 2-D variations in structure (see the supporting information). Path lengths are short relative to wavelengths for the iMUSH data set, so finite-frequency kernels have widths that are a significant fraction of path length and their accurate characterization produces clear improvement over ray theory. Tomographic inversions are stabilized via a first-derivative smoothness constraint and a weak norm-damping constraint, following standard damped-least squares methodologies (Menke, 1989). This approach leads to two regularization parameters, one controlling smoothing (γ) and the other controlling the norm damping (ε). We set ε sufficiently small so that the norm damping has minimal effect except where data are largely absent. The frequency-dependent parameter γ was determined by generalized cross-validation (Golub et al., 1979; Yao & Roberts, 1999) as described in the supporting information. Formal uncertainty for the ambient noise tomography is calculated as part of the inversion (Menke, 1989) and shown in Figures 5d and 5e.

3.5. Inversion for Shear Velocities (Vs)

The phase velocities from all single-frequency maps are combined for a dispersion curve at each 5 km $\times$ 5 km node. These curves are then inverted for $Vs(z)$ at each node with the same method as described in section 3.3, except that the starting model for individual nodes is now set to the $Vs_R(z)$ gradient model. Ambient noise and earthquake data are combined as described above and in Text S8. To balance the relative weights of the different data types in the $Vs(z)$ inversions, uncertainties for earthquake-based $c(\omega)$ were multiplied by five to be on average similar to the ambient noise uncertainties (Figure 5f). These two types of uncertainties are calculated with different assumptions, so the absolute uncertainties are not directly comparable. Inversions were run with both the gradient model and Moho model, to see the effect of the Moho smoothness constraint on results.
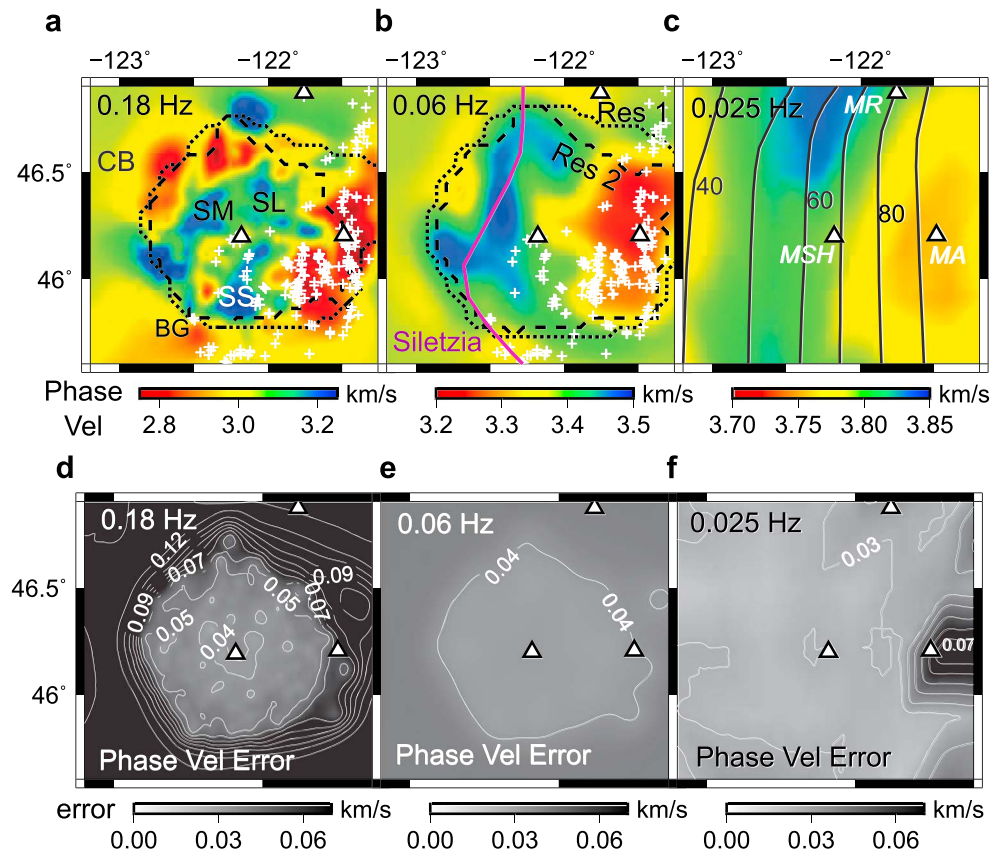
Figure 5. Phase velocity inversion results for three frequencies (a) 0.18 Hz, (b) 0.06 Hz, and (c) 0.025 Hz. (d–f) Formal resolution for (a)–(c), respectively. Panels (a), (b), (d), and (e) are based on ambient noise and (c) and (f) based on earthquakes; formal error for earthquakes (f) adjusted to match ambient noise as described in text. Maps include Quaternary vents from Hildreth (2007) (white crosses on a and b) and major volcanic edifices (white triangles, MSH, MA and MR). Other geologic features: (BG) Battle Ground maars, (CB) Chehalis Basin, (SM) Spud Mountain pluton, (SL) Spirit Lake pluton, and (SS) Silver Star pluton. On (b), purple line denotes east edge of Siletzia. On (c), lines show depths to slab surface. Resolution contours the same as Figure S4. Note that phase-velocity scale changes between panels.

4. Results

4.1. Phase Velocities in 2-D

4.1.1. Uncertainty

Formal 1-σ uncertainties for the ambient noise tomography phase velocity maps are 0.02–0.04 km/s within the region of best resolution (Figure S4). The "best resolution" region is defined as that where resolution matrix diagonals are >20% of their maximum value (Text S5). Formal uncertainties are slightly lower at higher frequencies; at 0.18 Hz the uncertainty is 0.02–0.03 km/s, and at 0.06 Hz it is 0.035–0.045 km/s. As a comparison, we also estimate uncertainties via bootstrap (Efron & Gong, 1983), repeating the phase-velocity inversions with randomly resampled sets of station pairs for 1,000 bootstrap trials. Within the area of best resolution, the standard deviation of the bootstrap trials is slightly lower than the formal error, by a factor of 1.4 at 0.06 Hz and 1.3 at 0.18 Hz. This suggests that formal errors slightly overestimate uncertainty but are quite close. The formal 1-σ uncertainties for earthquake surface-wave phase velocities are 0.007–0.015 km/s, calculated as described in section 3.2.2. For the Vs inversions, earthquake-based phase velocity errors are scaled up by 5 as discussed above (Figure 5f).

4.1.2. Resolution and Recovery Tests

To evaluate lateral resolution of the phase velocity images, we conduct a series of recovery tests on artificial data. Tests include checkerboard recovery and recovery of features that resemble those we interpret. In each test, the synthetic data are solved for with the same inversion parameters and data weights as the inversions of real data. First, we investigate the recovery of sharp lateral velocity steps across the array, such as those seen in the middle-lower crust (Figure 6), by inverting for an east-west 10% velocity step beneath the
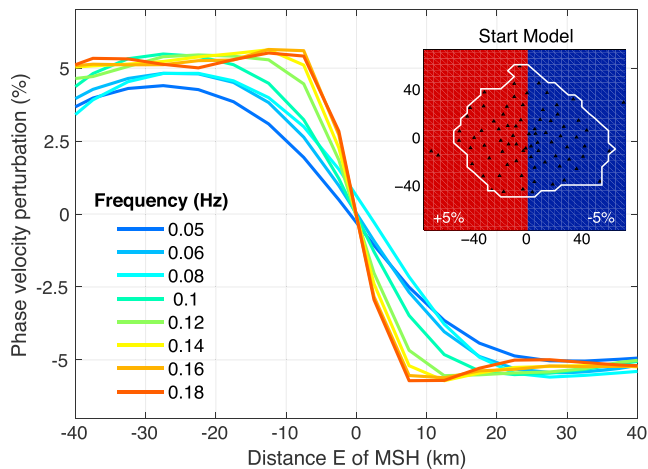
Figure 6. Recovery test of a 10% east-west step in phase velocity across Mount St. Helens (MSH), as a function of frequency as labeled. Model is shown in inset, coordinates centered at MSH. Inversion is for same inter-station paths and weights used with real data; on inset, triangles denote stations and white line denotes area of maximum resolution. Lines show resulting phase velocity variations along an east-west slice through the array center. Note trend toward full recovery away from the boundary (±5%), with a sharper boundary recovered at higher frequencies.

center of the array. The amplitude of this step is fully recovered at most frequencies, with the width of the transition between slow and fast velocities increasing from 10 km at 0.18 Hz to 30 km at 0.05 Hz, in both cases about half a wavelength. This test indicates that signal wavelength is limiting resolution within the array, emphasizing the importance of using finite-frequency kernels in the 2-D inversion.

Next, checkerboard tests explore anomalies varying by ±5% in between blocks, for block sizes of 15 and 50 km (Figure 7). A 50-km × 50-km anomaly has up to 100% amplitude recovery at 0.18 Hz and 90% amplitude recovery at 0.05 Hz. The 15-km × 15-km blocks have up to 90% amplitude recovery at 0.18 Hz and only 10% recovery at 0.05 Hz. These inversions recover features of a size approximately equal to the wavelength of the fundamental-mode Rayleigh waves, again emphasizing that the resolution of these images can be directly inferred from signal wavelength.

We explore additional feature-recovery tests to see if small bodies such as melt zones or magma chambers can be resolved with geometries postulated for the MSH plumbing system. These are shown in the supporting information and generally confirm that recovery is limited by wavelength of fundamental-mode Rayleigh waves — features as small as 5 km across may be resolved in the upper crust, but features 10 km across may be difficult to resolve in the lower crust.

4.1.3. Phase Velocity Anomalies

Figure 5 shows phase-velocity maps for three frequencies. The sensitivity kernels at 0.18, 0.06, and 0.025 Hz have a maximum sensitivity at 8-, 15-, and 45-km depth, respectively, although each is sensitive to *Vs* over a broad depth range (Figure 4a). At 0.18 Hz (Figure 5a), which samples the upper crust, low velocities spatially correlate with the location of the main volcanic arc to the east (e.g., Mount Adams) and sedimentary basins (e.g., the Chehalis Basin) to the northwest. Several plutons (labeled SM, SL, SS on Figure 5) correlate with high-velocity features, and volcanic vents generally correlate with low velocities, as discussed below. At 0.06 Hz (Figure 5b), which samples the midcrust, a sharp transition is observed between high velocities to the west and low velocities to the east. This transition likely delineates the eastern boundary between Siletzia and the region overlain by surface volcanic vents. The transition from high to low velocities lies near the longitude of MSH, with total E-W phase velocity variations of 8%. Finally, at 0.025 Hz (Figure 5c), which is most sensitive to uppermost mantle and lower crust, we observe a smoothed version of the same east-west velocity gradient as seen at 0.06 Hz.

4.2. 3-D *Vs* Variations

4.2.1. *Vs* Uncertainty

Uncertainties in the nonlinear *Vs* inversions for each grid node are estimated via Monte Carlo tests, as described in section 3.3 for $Vs_R(z)$. In the well-resolved parts of the model, these 1-σ uncertainties are 0.1–0.15, 0.06–0.11, and 0.08–0.12 km/s in the shallow crust (0- to 7.5-km depth), midcrust (15- to 25-km depth), and upper mantle (45- to 60-km depth), respectively. By comparison, *Vs* perturbations reach 0.3–0.4 and 0.3 km/s in the upper and midcrust and 0.2 km/s in the upper mantle so are much larger than these *Vs* uncertainties.

4.2.2. Vertical Resolution

Recovery tests investigate resolvability of a low-velocity layer at various depths (Figure 8). Phase velocities are predicted for a 1-D *Vs* model in which *Vs* is perturbed by −0.5 km/s in a layer 20 km thick superimposed on the reference model at a series of target depths. The model dispersion curve is then inverted in the same manner as real data with the same data weights, after adding ±0.05 km/s random noise. The three modeled low-velocity zones have tops at 5-, 15-, and 37.5-km depth (Figures 8a–8c), representing two crustal low-velocity zones and one just below the Moho, respectively. The shallower two are recovered to full amplitude although broadened in depth, while amplitude recovery for the 37.5-km zone is only 60%, and the perturbation extends to at least 20 km deeper than in the input model. These tests indicate that a crustal feature would be easily resolvable, but a feature in the upper mantle such as a mantle wedge or a subducting oceanic crust may be only partly recovered.
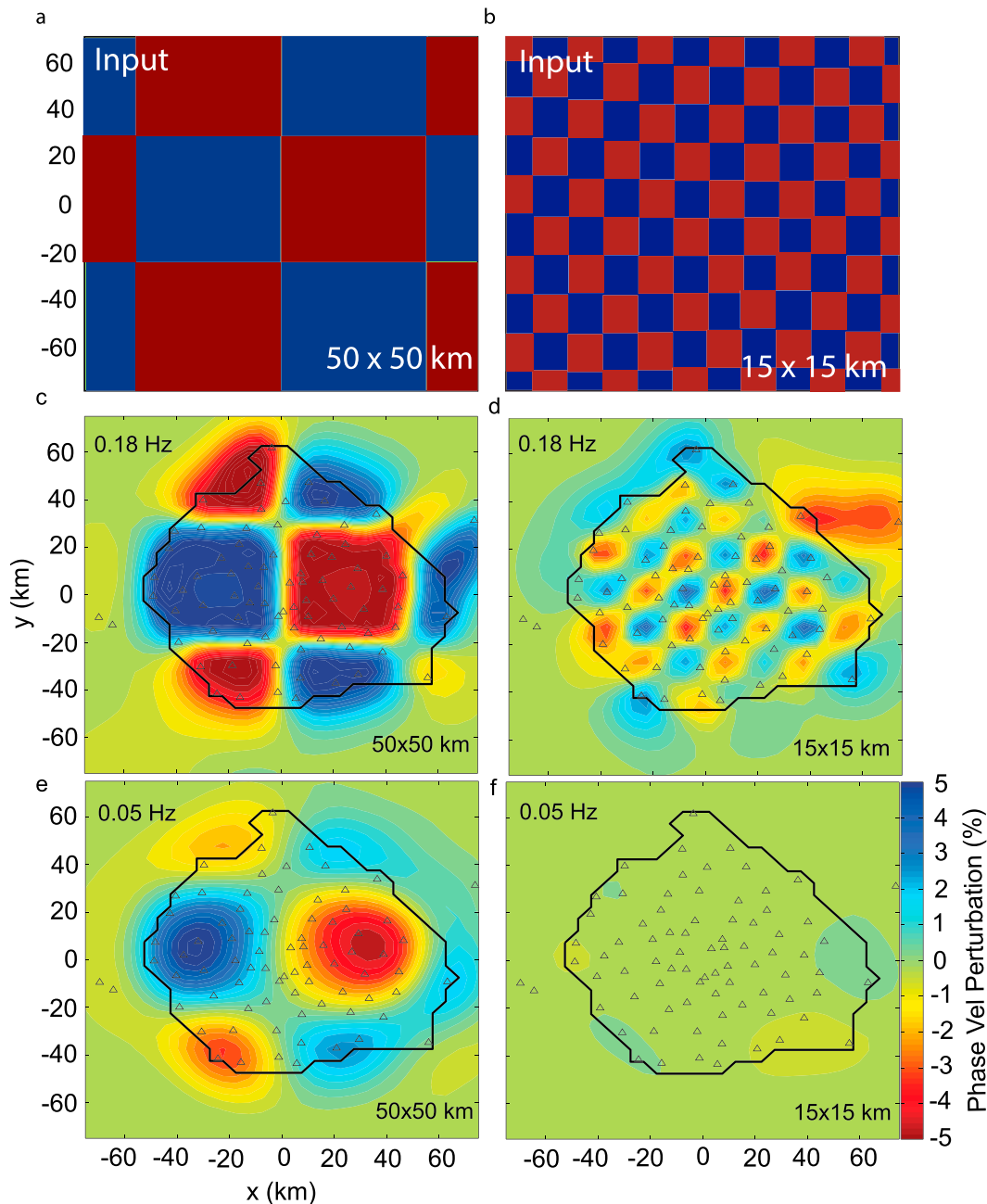
Figure 7. Checkerboard tests for two frequencies, 0.18 and 0.05 Hz, and (a and b) input block sizes, 15 and 50 km, for ±5% deviation in phase velocity. (c and d) Output from the resolution test for 0.18 Hz. (e and f) Output at 0.05 Hz. Black outline is the extent of high resolution from 0.1 Hz.

4.2.3. 3-D *Vs* Anomalies

For the gradient model (Figure 9) *Vs* lies in the range 3.45–3.95–km/s at 10- to 30-km depth and 4.0–4.4 km/s in the upper mantle (40- to 60-km depth). Figure S9 shows the full model. The Moho model is similar at all depths except near the Moho discontinuity and fits the data similarly (root mean square misfit is 31.6 m/s vs. 31.7 m/s for the gradient model), so we primarily show results from the gradient model. Previous studies similarly give *Vs* of 3.6–3.9 km/s at 10- to 30-km depth in the Cascadia forearc (Calkins et al., 2011), consistent with our result. Compared to previous seismic studies based on data from regional arrays (Gao & Shen, 2014; Porritt et al., 2011; Shen & Ritzwoller, 2016), resolution of the crust is significantly enhanced in our study (Figure 10). In particular, none of the previous studies resolve the sharp west-to-east transition from fast forearc to slow arc/backarc crust at the longitude of MSH, a primary result of this study. Several past
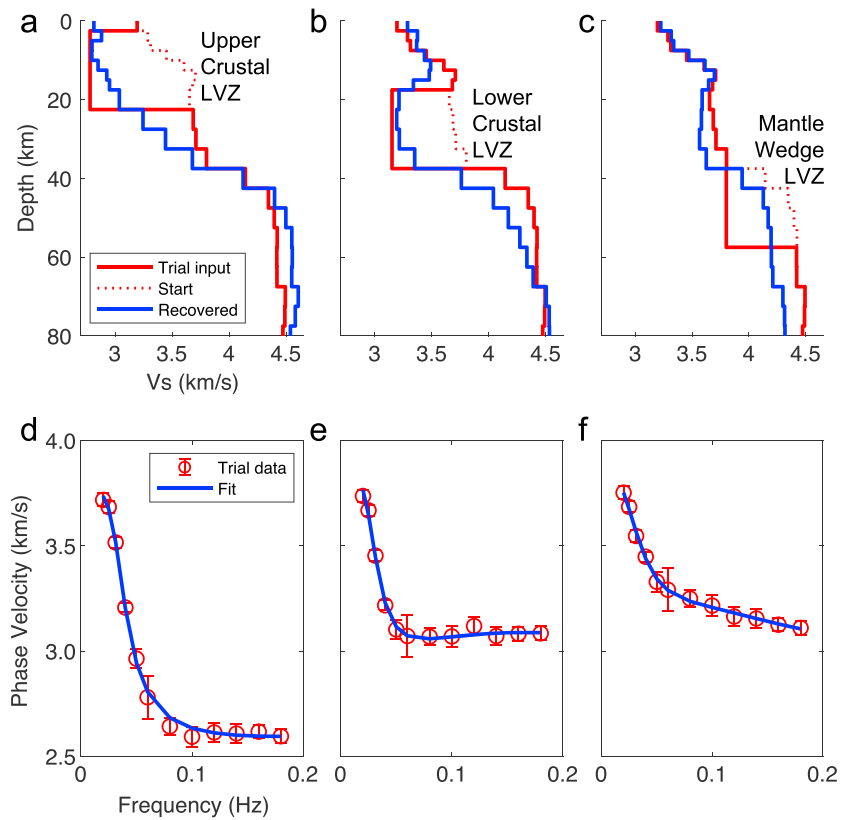
Figure 8. Recovery tests for inversions for *Vs* as a function of depth. (a–c) Velocity for starting model (dashed red line, same as solid black in Figure 4b), synthetic input model (solid red line), and the resulting model from inversion (blue). In each a 20 km thick, 0.5 km/s slow low-velocity zone (LVZ) is added to this starting model, as described in text, with top at 5, 15, and 37.5 km for (a)–(c), respectively. (d–f) Phase velocities for synthetic input model (red circles) and best fit after inversion (blue line).

studies show local differences in anomaly sign. Without a full analysis of these regional inversions, it is not clear why that is the case, but it is likely that sharp transitions between backarc, arc, forearc and the continent-ocean boundary are difficult to characterize at sparse station spacing.

In the middle-to-lower crust (Figures 9c, 9f, and 9g), features of minimum dimension 20–30 km should be resolvable given the wavelengths of the relevant signals. These depths show fast *Vs* of 4.0 $\pm$ 0.1 km/s at 15-km depth decreasing to 3.85 $\pm$ 0.09 km/s at 30-km depth, everywhere west of MSH (Figures 9c, 9e, and 9g). Global averages for continental *Vs* are 3.4–3.7 km/s for these depths, combining *Vp* compilations (Christensen & Mooney, 1995) with common *Vs-Vp* relationships (Brocher, 2005). Within the contiguous United States, midcrustal *Vs* from ambient noise inversions are commonly 3.5–3.8 km/s (Shen & Ritzwoller, 2016). Near Mount Rainier, Obrebski et al. (2015) show lower-crustal *Vs* of 3.60–3.85 km/s, while Flinders and Shen (2017) show *Vs* of 3.7–3.9 km/s at similar depths at the longitude of MSH. Our observations are slightly faster than most of these regional measures.

Lower *Vs* (3.5–3.65 km/s) is imaged at 15- to 30-km depths in much of the 50-km-wide region between MSH and Mount Adams (Figures 9c and 9g). The distribution of this feature correlates at 30-km depth with the Southern Washington Cascades Conductor (Bedrosian et al., 2018; Hill et al., 2009; Stanley et al., 1987) and partly correlates at 20-km depth. Low *P* wave velocities here are also seen in active-source imaging (Kiser et al., 2016). The Quaternary vent field near also correlates quantitatively with the low-*Vs* region at 20–30 km. Specifically, of the 177 identified vents in the well-resolved part of the model (Figures 9b and 9c), 108 of them are in the slowest 50% of the model at 20-km depth. The probability of 108 matches in 177 trials being random (50% probability of individual matches) is 0.1%. Given this geometry and correlation, it seems likely that the low *Vs* region is genetically related to Quaternary volcanism (Bedrosian et al., 2018).
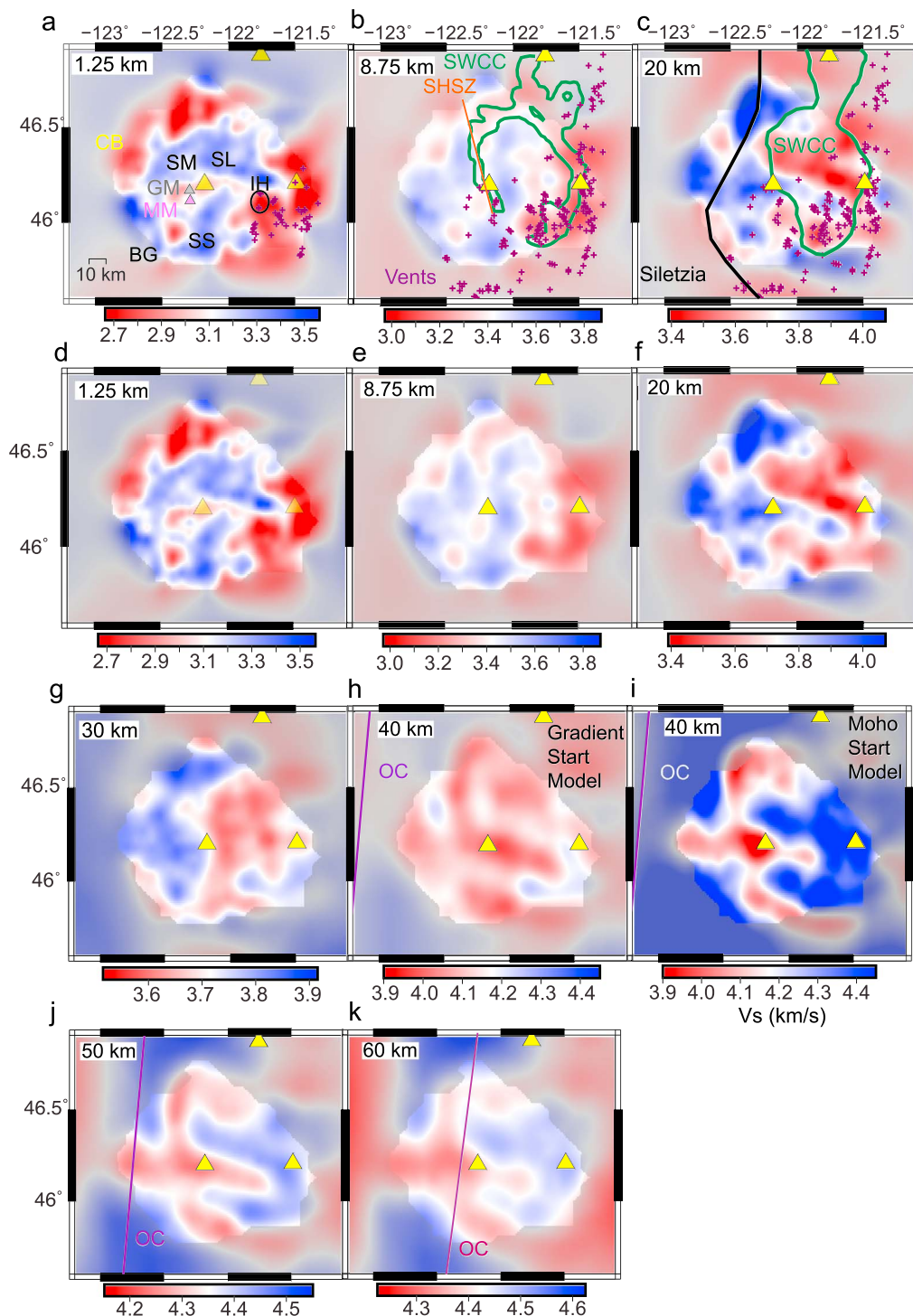
Figure 9. Maps of *Vs* for the gradient model. (a) Model for upper crust (0- to 2.5-km depth) with geological features labeled: Chehalis basin (CB), Spirit Lake pluton (SL), Spud Mountain pluton (SM), Battle Ground Maar (BG), Silver Star pluton (SS), Goat Mountain (GM), and Marble Mountain (MM); the last two are gray and pink triangles, respectively (Hildreth, 2007; Schuster, 2005). SWCC is Southern Washington Cascades Conductor (Stanley et al., 1987). (b) Model for 7.5- to 10-km depth, showing (orange) the SHZ and (green outline) high conductivity body at 7-km depth (Bedrosian et al., 2018). (c) Model at 20-km depth, along with (black) Siletzia terrane boundary (Wells et al., 2014) and (green outline) high-conductivity body at 24-km depth (Bedrosian et al., 2018). In (a)–(c), Quaternary vents are purple crosses. (d–f) Same as (a)–(c) but without annotations. (g) Gradient model at 30-km depth. (h) Gradient model at 40-km depth. (i) Same as (h) but with Moho model. (j) Gradient model at 50-km depth. (k) Gradient model at 60-km depth. In (h)–(k), purple contour shows the subducting oceanic crust (OC) at this depth, from Mann et al. (2019). Yellow triangles show major volcanoes. All velocities are masked by the region of high resolution for 0.1-Hz phase velocity inversions (see Figure S4).
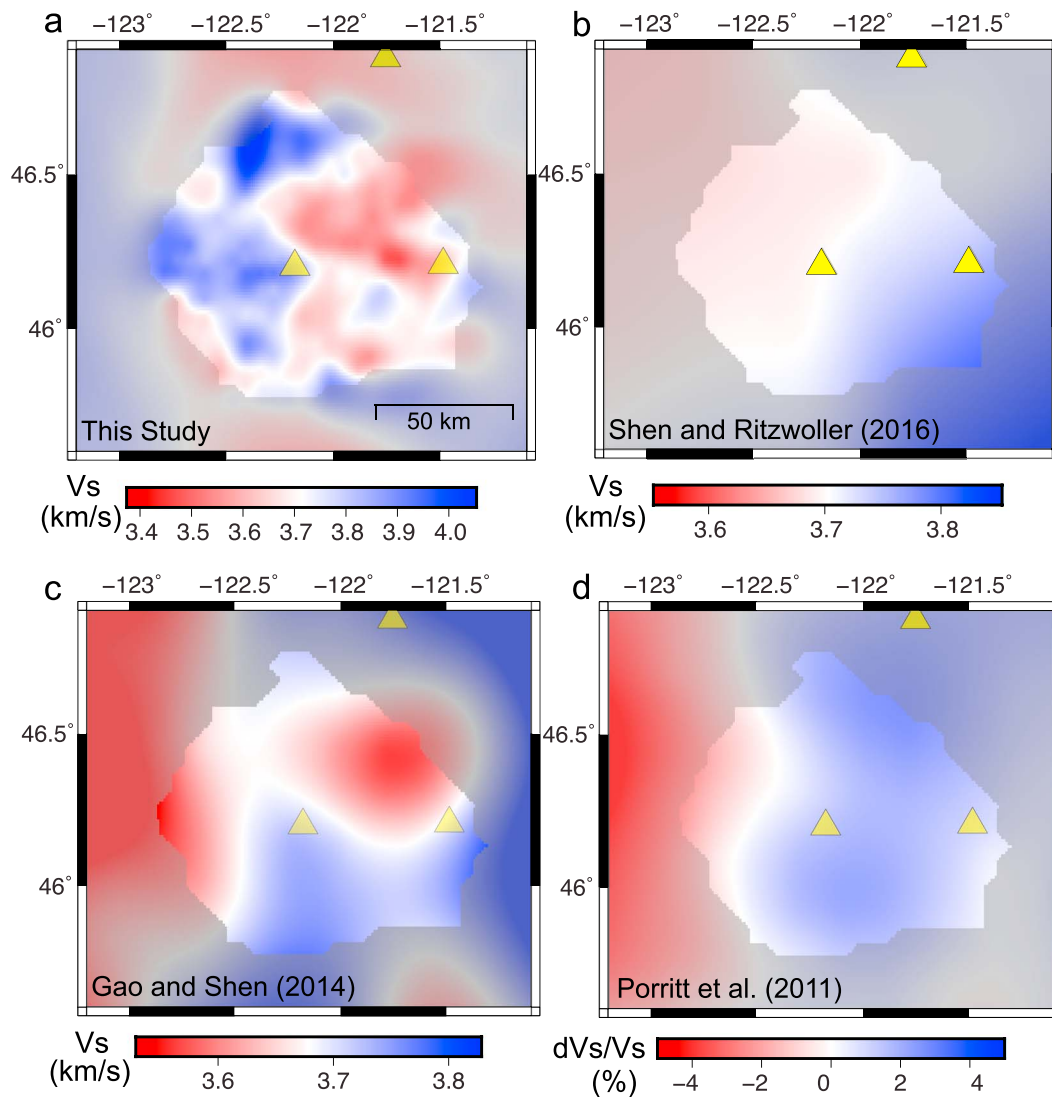
Figure 10. Comparison of *Vs* at 25-km depth between this paper and several previously published regional models. (a) This study; (b) Shen and Ritzwoller (2016); (c) Gao and Shen (2014); (d) Porritt et al. (2011). Yellow triangles show major volcanoes. *Vs* is masked by the same resolution contour as in Figure 9.

A similar conclusion was reached by Flinders and Shen (2017), who imaged the northern half of our study region in their lower-resolution regional full-waveform tomography.

In the uppermost mantle the absolute *Vs* is somewhat dependent on choice of starting model and smoothness condition on the Moho (cf. Figures 9h and 9i, 11c and 11d, and Figure S7), although relative *Vs* patterns are stable and the forearc is consistently slower than farther east. Most upper mantle *Vs* values are 4.2–4.5 km/s, similar to observations beneath Mount Rainier (Obrebski et al., 2015). The higher values, observed east of MSH and near Mount Adams, resemble typical regional (Shen & Ritzwoller, 2016) and global (Christensen & Mooney, 1995) upper-mantle *Vs*. The lowest uppermost-mantle velocities are seen west of MSH in the shallow forearc. These data do not obviously image the deeper subducting plate.

5. Discussion

5.1. Upper Crust

At shallow depths (<10 km) the *Vs* variations correspond well to geologic features (Figures 9a and 9b). Low *Vs* at the western edge of the array (2.7 ± 0.1 km/s at 0- to 2.5-km depth) corresponds to the Chehalis Basin (e.g., Stanley et al., 1996). High *Vs* is locally found NE, NW, and S of MSH where Tertiary Spirit Lake, Spud
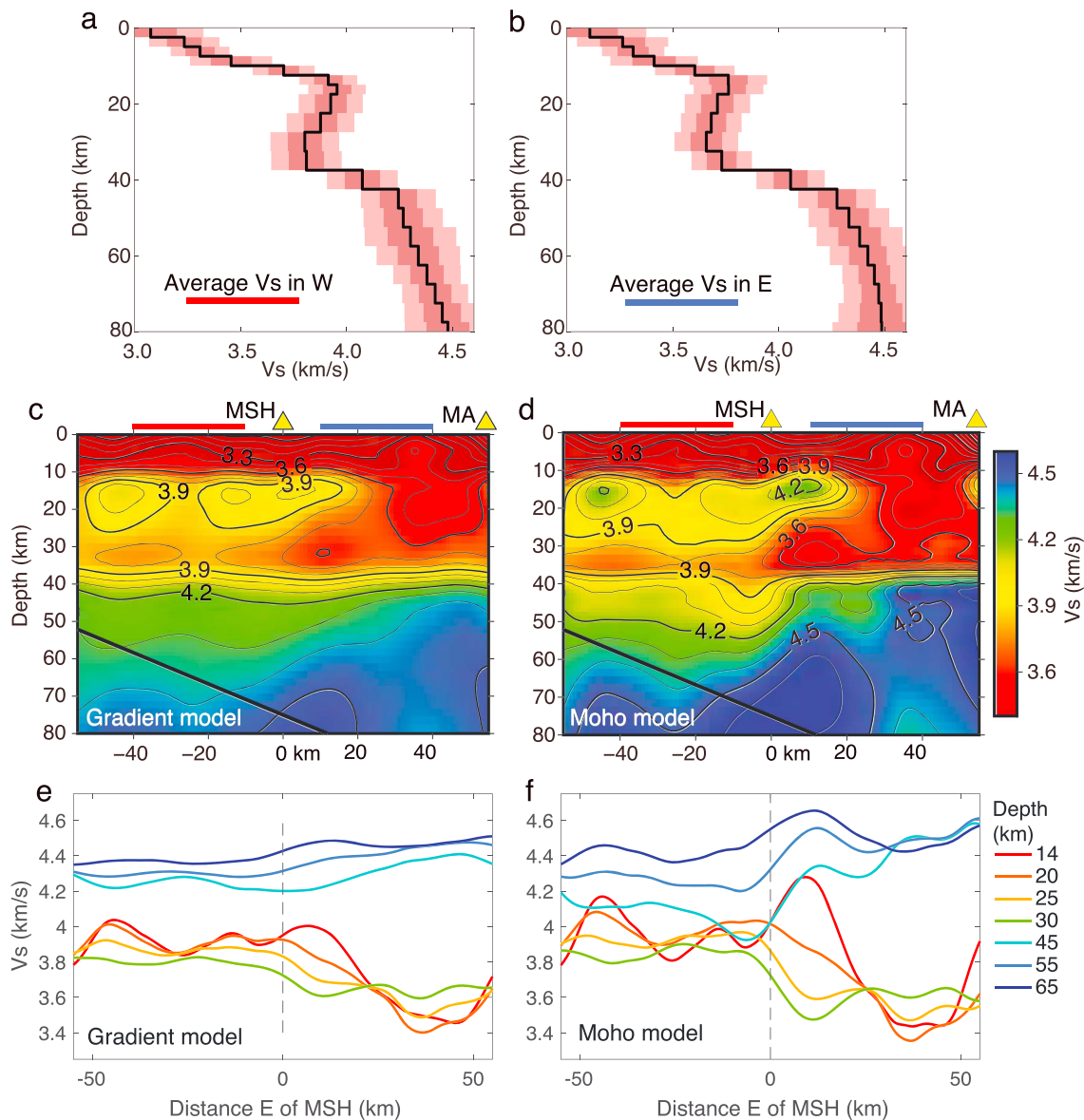
Figure 11. East-west transect through Mount St. Helens (MSH). (a) Average *Vs* variation with depth in the west/forearc, in a 30 × 30 km box centered 25 km due west of MSH (Figure 2 and red bar on c). Black line: averaged velocity; dark and light shaded area: 1- and 2-σ uncertainty from Monte Carlo, respectively. (b) Same for a 30 × 30 km average centered 25 km due east of MSH (Figure 2 and blue bar on c). (c) E-W *Vs* transect through the gradient model passing through MSH. Black line shows oceanic Moho from Mann et al. (2019); plate interface is 6 km shallower. (d) Same for the Moho model. Velocity scale on right. (e and f) *Vs* at different depths as labeled, taken from the same data as panes (c) and (d), for gradient and Moho model, respectively.

Mountain, and Silver Star plutons are exposed (e.g., Schuster, 2005). This ring of high velocities shows *Vs* of 3.40 ± 0.15 km/s and resembles features seen in full-waveform tomography (Flinders & Shen, 2017). These same plutons and sedimentary basins are visible in local-earthquake *P* wave tomography (e.g., Lees & Crosson, 1989; Moran et al., 1999; Ulberg et al., 2017; Waite & Moran, 2009), all of whom also show a low-velocity zone along the St. Helens seismic zone (SHZ; Weaver & Smith, 1983) northwest of MSH (Figure 9b). An upper-crustal high-conductivity anomaly also passes through MSH and the SHZ (Bedrosian et al., 2018). The SHZ is weakly imaged with a low amplitude of −3% in our results.

A low-velocity feature extending 35 km southwest of MSH has velocities of 2.8 + 0.13 km/s at <3-km depth. This feature correlates with a handful of vents that extend from Battle Ground maar in the SW to MSH (BG in Figure 5a; Hildreth, 2007). Lees and Crosson (1989) image a similar low-velocity feature near MSH, but

our well-resolved feature extends farther south and suggests a larger, continuous feature that incorporates all the vents southwest of MSH. In the southeast, a large low-velocity feature (Vs = 2.7 ± 0.11 km/s) corresponds well with the Indian Heaven—Mount Adams region of abundant Quaternary vents. Although these vents are largely basaltic (Hildreth, 2007), their Vs is low in the upper crust and likely reflects the altered and porous nature of the volcanic cover.

5.2. Absence of Moho Beneath the Forearc

The Moho discontinuity disappears within a couple kilometers west of the MSH edifice in Pn amplitudes (Brocher et al., 2003), PmP reflections (Hansen et al., 2016), and receiver functions (Mann et al., 2019). Likewise, the surface-wave tomography presented here shows steep velocity gradients across the Moho to the east and very weak velocity gradients in the west, although the amplitude of the Moho step is sensitive to the initial model (Figures 11 and S9). The Moho Vs step is estimated as the difference in Vs within 10 km of the discontinuity, that is, from 27.5- to 47.5-km depth. With this criterion, the gradient model shows a Vs step across the Moho of ≤0.3 km/s in the west compared with 0.85 km/s in the east, whereas the Moho model shows a Vs step of 0.1 km/s in the west compared with 0.9 km/s in the east. Thus, the weak-to-absent forearc Moho is a robust feature in these results. Because this approach estimates the Moho step over 20 km where other pressure-dependent Vs increases likely occur, the absolute step estimates are likely overestimates, but the relative variations should be robust. Inspection of the velocities shows the weak forearc Moho is a result of both a high Vs in the lower crust and a low uppermost-mantle Vs, with the change in lower-crustal Vs being larger.

Previous studies have inferred that the Moho reduction is entirely due to a slow, serpentinized forearc mantle wedge (Bostock et al., 2002; Brocher et al., 2003; Hansen et al., 2016). However, they only constrain velocity or impedance contrasts rather than absolute velocities, so they cannot distinguish low upper-mantle velocities from high lower-crustal velocities. A fully hydrated forearc mantle wedge would have Vs ~ 4.0–4.1 km/s (Abers et al., 2017; Reynard, 2013), with antigorite serpentine and chlorite as the main hydrous phases affecting Vs. These predictions are somewhat slower than the $Vs \geq$ 4.2 km/s imaged here (Figure 11), although decreased resolution at these depths may attenuate anomalies (Figures 8c). However, even a fully hydrated forearc mantle wedge should still show a measurable velocity contrast with "normal" crust (Vs ~ 3.5–3.8 km/s). The strong westward increase in crustal velocities to nearly 4.0 km/s just west of MSH is clearly necessary to explain the absence of a forearc Moho; mantle wedge hydration alone is insufficient to produce this observation. These observations in Cascadia of an invisible forearc Moho are among the primary observations worldwide that have been used to argue for extensive forearc serpentinization, as argued by Hyndman and Peacock (2003). Our crustal velocity estimates call for reevaluation of the notion that forearcs are extensively serpentinized (see also Abers et al., 2017).

5.3. Lower Crust in the Forearc: Siletzia?

The fast middle-lower crust in the west of the study area abruptly ends at the longitude of MSH (Figures 9c and 9g) and has Vs of 3.95 ± 0.1 km/s at 20- to 30-km depth. The distribution and seismic properties of the fast middle-lower crust correspond to the eastward extent of the gabbroic Siletzia terrane. We image this boundary within a couple kilometers of MSH similar to a wide-angle seismic line that indicates that MSH and the SHZ lie directly on the eastern Siletz limit (Parsons et al., 1998; Figure 9c). By contrast, teleseismic traveltime inversions have been used to infer that Siletzia extends hundreds of kilometers farther east of MSH (Schmandt & Humphreys, 2011); we infer that the teleseismic result involves only the mantle lithosphere and not Siletz crust.

To quantify the extent to which composition explains the lateral velocity variations of the lower crust, we calculate Vs at a range of temperatures consistent with surface heat flow for Siletz gabbro compositions, following the calculation of Till et al. (2019). Forearc heat flow of 34 ± 4 mW/m^2 (see the supporting information) is extrapolated to midcrustal depths for an assumed thermal conductivity of 2.0 ± 0.5 W/m/K (Pollack et al., 1993; van Keken et al., 2018). Heat production in gabbros should be negligible and the crust appears to be in thermal steady state so a linear geotherm is appropriate (Till et al., 2019). The resulting temperatures are then used to calculate Vs at depth in the forearc from petrologic models (Figure 12). Specifically, we estimate modal mineralogy from major element oxide compositions for a suite of 16 samples of the Crescent-Siletz basalt (Phillips et al., 2017; Sisson et al., 2014) using the Perple_X free-energy minimization
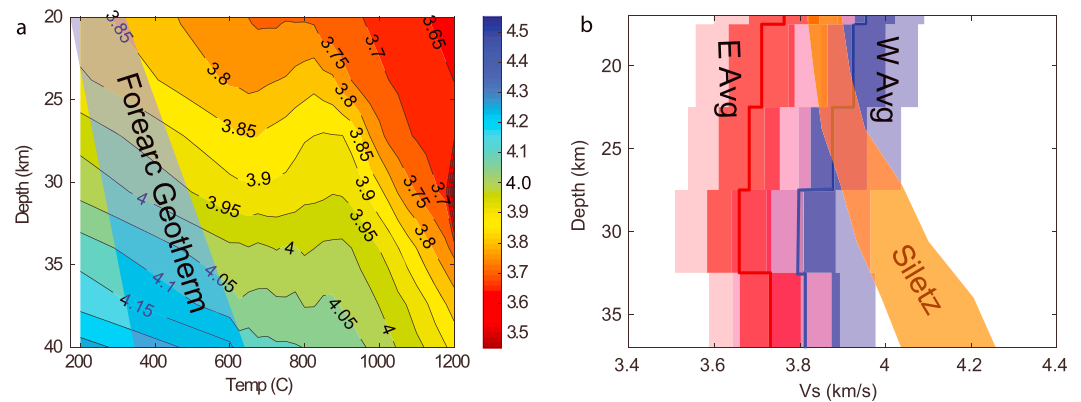
Figure 12. (a) Estimates of *Vs* averaged for samples of Siletz-Crescent basalts, calculated at a range of temperature and pressures/depths, along with the allowed range of forearc temperatures, as described in text. (b) Comparison of this predicted *Vs* versus depth for Siletzia within the forearc geotherms (orange), with average observed *Vs* east (red) and west (blue) of Mount St. Helens. Shading and lines correspond with Figures 11a and 11b for a and b, respectively.

algorithm (Connolly, 2005) and parameters described previously (Obrebski et al., 2015; Till et al., 2019). From these compositions we calculate *Vs* as a function of pressure and temperature following Abers and Hacker (2016); Figure 12a. For the range of plausible forearc geotherms, *Vs* is predicted to increase from 3.85 ± 0.05 km/s at 20-km depth to 4.00 ± 0.10 km/s at 30-km depth. This agrees well with our estimated *Vs* values in this area (Figure 12b). At depths between 30 km and the Moho, the observed *Vs* is systematically less than the predicted Siletz *Vs*, but the discrepancy is small. Given the overall agreement, it seems likely that Siletzia makes up the basement west of MSH. Because these high velocities end abruptly at MSH and are not imaged farther east, the Siletzia terrane likely ends at MSH (Figure 13).
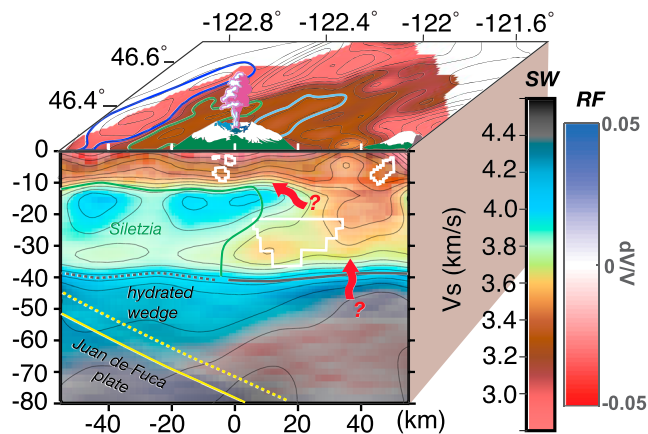
5.4. Melt Pathways to MSH

Figure 13. Schematic interpretation of the *Vs* model. Vertical slice follows Figure 11c, and top surface shows *Vs* at 2.5-km depth. Blue/red shading overlay on cross-section shows migrated receiver function image of Mann et al. (2019). Colors on vertical slice are shaded combination of the surface-wave color scale (SW) and that for receiver functions (RF). Outlines on top surface show Chehalis basin (dark blue) and major plutons (light blue). Other features include the 15-Ω contour of the electrically conductive body (Bedrosian et al., 2018), white; inferred extent of Siletzia, green; the Moho and top surface of subducting Juan de Fuca Plate, solid and dashed yellow, respectively; and inferred upper-plate Moho, black and dashed where absent to receiver functions. Red arrows show one possible melt transport pathway from the hot mantle wedge to Mount St. Helens, limited westward by the boundary of Siletzia.

One explanation for the location of MSH is that the Siletzia terrane acts as a westward barrier to magma migration in the crust (Figure 13). This inference is consistent with recent images of conductivity structures, which show a complex conductive body that partly follows the Siletz eastern margin at upper-crustal depths and lies farther east at midcrustal depths (Bedrosian et al., 2018). The close coincidence between the eastern boundary of the high-velocity crust (Siletzia) and MSH provides strong indication that crustal structure controls magma pathways.

It is less clear where the melt forms. Blatter et al. (2017) conclude that dacites typical of MSH eruptions last equilibrated from depths of 25–30 km at temperatures of 925–940 °C, indicating the presence of an extensive region of partial melt just above the Moho somewhere beneath MSH. Evidence suggests that this melt region may be offset from the edifice; for example, low upper-mantle velocities in the forearc indicate some hydration as discussed above, requiring temperatures there to be <800 °C (Abers et al., 2017), which are inconsistent with higher temperatures in the overlying crust. In map view (Figure 9c) the crust has significantly lower *Vs* east of MSH than west of it (3.45–3.7 km/s at 15- to 25-km depth). The low-*Vs* region imaged at 20- to 30-km depth between MSH and Mount Adams is similar in shape and location to a pronounced lower-crustal conductor (Bedrosian et al., 2018; Hill et al., 2009) and likely indicates the same feature. The conductor is inferred to contain several percent dacitic melt (Bedrosian et al., 2018).

The observation of *Vs* < 3.6 km/s in the lower crust is difficult to explain by composition alone. While the basement composition beneath the

Cascades is poorly known, Obrebski et al. (2015) show Vs is relatively insensitive to silica content for a wide range of intermediate-to-felsic compositions, based on the compositional compilation of Jagoutz and Behn (2013). At 550 °C and 0.8 GPa, they show that Vs lies near 3.8 km/s, and never below 3.7 km/s. While temperature variations are poorly known for these compositions, owing to the competing effects of thermal expansion and dehydration-mediated reactions, most direct calculations on dry felsic rocks are unable to produce $Vs < 3.6$ km/s (e.g., Abers et al., 2016; Brownlee et al., 2011). Across the United States, at 25-km depth Vs is less than 3.6 km/s in only 3.4% of the area resolved by Shen and Ritzwoller (2016), largely beneath volcanic areas of the Cascades or Basin and Range. Thus, it seems most likely that some melt contributes to the low Vs seen between Mount Adams and MSH. Analyzing the percentage partial melt present is beyond the scope of this paper because melt effects on felsic rocks are complex, the starting composition is poorly known, and other factors such as water content of the melt may have strong effects. However, melt contents of a few percent have been inferred from resistivity (Bedrosian et al., 2018) and seem plausible.

Regardless, the low-Vs anomaly and high-conductivity features are associated with abundant diffuse Quaternary volcanism between MSH and Mount Adams. While the direct linkages to MSH cannot be imaged at the resolution of this study, these connections and the petrological evidence for high lower crustal temperatures make it likely that a small partial melt body in the lower crust is displaced from the MSH edifice, probably eastward. Volcanism beneath Indian Heaven or Mount Adams is easier to reconcile with crustal Vs immediately beneath those Quaternary centers.

6. Conclusions

The dense iMUSH array enables several new observations and inferences:

1. Ambient noise tomography works effectively for relatively small, dense arrays like iMUSH at depths shallower than 50–60 km. Image resolution is fundamentally limited by the wavelengths of the relevant signals, not station spacing, although array aperture limits the largest recoverable wavelengths. This is one of the first arrays of sufficient density and areal extent to demonstrate such resolution.
2. The observed absence of a Moho above the forearc mantle is consistent with Vs images from this study, which constrains absolute Vs. The Moho vanishes both because of the high-Vs (and presumably Vp) crust above the forearc mantle (3.95 ± 0.1 km/s) and the low-velocity, hydrated mantle wedge, which has a similar Vs near 4.1 km/s; hydration alone cannot produce this effect. An understanding of upper plate geology is necessary in order to interpret hydration from Moho properties.
3. The Siletzia terrane makes up the middle and lower crust everywhere west of MSH, where it abruptly ends. Its boundary coincides with MSH and the eastern edge of the low forearc heat flow province and could be an explanation for the specific location of the volcanic edifice; the terrane may act as a westward barrier for volcanism. The east edge of Siletzia may correspond with volcano locations in nearby parts of Cascadia as well (Figure 1), although other factors such as the depth to slab and resultant thermal structure may be more important regionally.
4. The Vs between the main volcanoes (MSH, Mount Rainier, Indian Heaven, and Mount Adams) may require partial melt, at least at lower-crustal depths. The lowest Vs features coincide well with resistivity anomalies and indicate a regional rather than local crustal source for this magmatism.

References

Abers, G. A., Eilon, Z., Gaherty, J. B., Jin, G., Kim, Y. H., Obrebski, M., & Dieck, C. (2016). Southeast Papuan crustal tectonics: Imaging extension and buoyancy of an active rift. *Journal of Geophysical Research: Solid Earth*, *121*, 951–971. https://doi.org/10.1002/2015JB012621

Abers, G. A., & Hacker, B. R. (2016). A MATLAB toolbox and Excel workbook for calculating the densities, seismic wave speeds, and major element composition of minerals and rocks at pressure and temperature. *Geochemistry, Geophysics, Geosystems*, *17*, 616–624. https://doi.org/10.1002/2015GC006171

Abers, G. A., van Keken, P. E., & Hacker, B. R. (2017). The cold and relatively dry nature of mantle forearcs in subduction zones. *Nature Geoscience*, *10*(5), 333–337. https://doi.org/10.1038/ngeo2922

Accardo, N. J., Gaherty, J. B., Shillington, D. J., Ebinger, C. J., Nyblade, A. A., Mbogoni, G. J., et al. (2017). Surface wave imaging of the weakly extended Malawi Rift from ambient-noise and teleseismic Rayleigh waves from onshore and lake-bottom seismometers. *Geophysical Journal International*, *209*(3), 1892–1905. https://doi.org/10.1093/gji/ggx133

Aki, K. (1957). Space and time spectra of stationary stochastic waves, with special reference to microtremors. *Bulletin. Earthquake Research Institute, University of Tokyo*, *35*, 415–456.

Bedrosian, P. A., Peacock, J. R., Bowles-Martinez, E., Schultz, A., & Hill, G. J. (2018). Crustal inheritance and a top-down control on arc magmatism at Mount St Helens. *National Geoscience*, *11*(11), 865–870. https://doi.org/10.1038/s41561-018-0217-2

Bensen, G. D., Ritzwoller, M. H., Barmin, M. P., Levshin, A. L., Lin, F., Moschetti, M. P., et al. (2007). Processing seismic ambient noise data to obtain reliable broad-band surface wave dispersion measurements. *Geophysical Journal International*, *169*(3), 1239–1260. https://doi.org/10.1111/j.1365-246X.2007.03374.x

Blackwell, D. D., Steele, J. L., Kelley, S., & Korosec, M. A. (1990). Heat flow in the state of Washington and thermal conditions in the Cascade Range. *Journal of Geophysical Research*, *95*(B12), 19,419–495,516.

Blakely, R. J., Brocher, T. M., & Wells, R. E. (2005). Subduction-zone magnetic anomalies and implications for hydrated forearc mantle. *Geology*, *33*(6), 445–448. https://doi.org/10.1130/G21447.1

Blatter, D. L., Sisson, T. W., & Hankins, W. B. (2017). Voluminous arc dacites as amphibole reaction-boundary liquids. *Contributions to Mineralogy and Petrology*, *172*(5), 26–37. https://doi.org/10.1007/s00410-017-1340-6

Bostock, M. G., Hyndman, R. D., Rondenay, S., & Peacock, S. M. (2002). An inverted continental Moho and serpentinization of the forearc mantle. *Nature*, *417*(6888), 536–538. https://doi.org/10.1038/417536a

Brocher, T. M. (2005). Empirical relations between elastic wavespeeds and density in the Earth's crust. *Bulletin of the Seismological Society of America*, *95*(6), 2081–2092. https://doi.org/10.1785/0120050077

Brocher, T. M., Parsons, T., Trehu, A. M., Snelson, C. M., & Fisher, M. A. (2003). Seismic evidence for widespread serpentinized forearc upper mantle along the Cascadia margin. *Geology*, *31*(3), 267–270. https://doi.org/10.1130/0091-7613

Brownlee, S. J., Hacker, B. R., Salisbury, M., Seward, G., Little, T. A., Baldwin, S. L., & Abers, G. A. (2011). Predicted velocity and density structure of the exhuming Papua New Guinea ultrahigh-pressure terrane. *Journal of Geophysical Research*, *116*, B08206. https://doi.org/10.1029/2011JB008195

Calkins, J. A., Abers, G. A., Ekstrm, G., Creager, K. C., & Rondenay, S. (2011). Shallow structure of the Cascadia subduction zone beneath western Washington from spectral ambient noise correlation. *Journal of Geophysical Research*, *116*, B07302. https://doi.org/10.1029/2010JB007657

Christensen, N. I., & Mooney, W. D. (1995). Seismic velocity structure and composition of the continental crust: A global view. *Journal of Geophysical Research*, *100*(B6), 9761–9788. https://doi.org/10.1029/95JB00259

Coney, P. J., Jones, D. L., & Monger, J. W. (1980). Cordilleran suspect terranes. *Nature*, *288*(5789), 329–333. https://doi.org/10.1038/288329a0

Connolly, J. A. (2005). Computation of phase equilibria by linear programming: A tool for geodynamic modeling and its application to subduction zone decarbonation. *Earth and Planetary Science Letters*, *236*(1-2), 524–541. https://doi.org/10.1016/j.epsl.2005.04.033

Crosbie, K. J. (2018). Shear velocity structure from ambient noise and teleseismic surface wave tomography in the Cascades around Mount St. Helens (M.S.). Cornell Univ., Ithaca.

De Siena, L., Thomas, C., Waite, G. P., Moran, S. C., & Klemme, S. (2014). Attenuation and scattering tomography of the deep plumbing system of Mount St. *Helens. Journal of Geophysical Research: Solid Earth*, *119*(11), 8223–8238.

Efron, B., & Gong, G. (1983). A leisurely look at the bootstrap, the jackknife, and cross-validation. *Amer. Statist.*, *37*, 36–48.

Ekström, G., Abers, G. A., & Webb, S. C. (2009). Determination of surface-wave phase velocities across USArray from noise and Aki's spectral formulation. *Geophysical Research Letters*, *36*, L18301. https://doi.org/10.1029/2009GL039131

Flinders, A. F., & Shen, Y. (2017). Seismic evidence for a possible deep crustal hot zone beneath Southwest Washington. *Scientific Reports*, *7*(1), 7400. https://doi.org/10.1038/s41598-017-07123-w

Gao, H., & Shen, Y. (2014). Upper mantle structure of the Cascades from full-wave ambient noise tomography: Evidence for 3D mantle upwelling in the back-arc. *Earth and Planetary Science Letters*, *390*, 222–233. https://doi.org/10.1016/j.epsl.2014.01.012

Golub, G. H., Heath, M., & Wahba, G. (1979). Generalized cross-validation as a method for choosing a good ridge parameter. *Technometrics*, *21*(2), 215–223. https://doi.org/10.1080/00401706.1979.10489751

Hansen, S. M., Schmandt, B., Levander, A., Kiser, E., Vidale, J. E., Abers, G. A., & Creager, K. C. (2016). Seismic evidence for a cold ser-pentinized mantle wedge beneath Mount St Helens. *Nature Communications*, *7*(1), 13242. https://doi.org/10.1038/ncomms13242

Harmon, N., Gerstoft, P., Rychert, C. A., Abers, G. A., de la Cruz, M. S., & Fischer, K. M. (2008). Phase velocities from seismic noise using beamforming and cross correlation in Costa Rica and Nicaragua. *Geophysical Research Letters*, *35*, L19303. https://doi.org/10.1029/2008GL035387

Herrmann, R. B. (2013). Computer programs in seismology: An evolving tool for instruction and research. *Seismological Research Letters*, *84*(6), 1081–1088. https://doi.org/10.1785/0220110096

Hildreth, W. (2007). Quaternary magmatism in the Cascades; geologic perspectives. In *U.S. Geological Survey Professional Paper 1744* (125 pp.).

Hill, G. J., Caldwell, T. G., Heise, W., Chertkoff, D. G., Bibby, H. M., Burgess, M. K., et al. (2009). Distribution of melt beneath Mount St Helens and Mount Adams inferred from magnetotelluric data. *Nature Geoscience*, *2*(11), 785–789. https://doi.org/10.1038/ngeo661

Hyndman, R. D., & Peacock, S. M. (2003). Serpentinization of the forearc mantle. *Earth and Planetary Science Letters*, *212*(3-4), 417–432. https://doi.org/10.1016/S0012-821X(03)00263-2

Hyndman, R. D., & Wang, K. (1993). Thermal constraints on the zone of major thrust earthquake failure: The Cascadia subduction zone. *Journal of Geophysical Research*, *98*(B2), 2039–2060. https://doi.org/10.1029/92JB02279

Jagoutz, O., & Behn, M. D. (2013). Foundering of lower island-arc crust as an explanation for the origin of the continental Moho. *Nature*, *504*(7478), 131–134. https://doi.org/10.1038/nature12758

Janiszewski, H. A., Gaherty, J. B., Abers, G. A., Gao, H., & Eilon, Z. C. (2019). Amphibious surface-wave phase-velocity measurements of the Cascadia subduction zone. *Geophysical Journal International*, *217*(3), 1929–1948. https://doi.org/10.1093/gji/ggz051

Jin, G., & Gaherty, J. B. (2015). Surface wave phase-velocity tomography based on multichannel cross-correlation. *Geophysical Journal International*, *201*(3), 1383–1398. https://doi.org/10.1093/gji/ggv079

Jin, G., Gaherty, J. B., Abers, G. A., Kim, Y., Eilon, Z., & Buck, R. W. (2015). Crust and upper mantle structure associated with extension in the Woodlark Rift, Papua New Guinea from Rayleigh-wave tomography. *Geochemistry, Geophysics, Geosystems*, *16*, 3808–3824. https://doi.org/10.1002/2015GC005840

Kiser, E., Levander, A., Zelt, C., Schmandt, B., & Hansen, S. (2018). Focusing of melt near the top of the Mount St. Helens (USA) magma reservoir and its relationship to major volcanic eruptions. *Geology*, *46*(9), 775–778. https://doi.org/10.1130/G45140.1

Kiser, E., Palomeras, I., Levander, A., Zelt, C., Harder, S., Schmandt, B., et al. (2016). Magma reservoirs from the upper crust to the Moho inferred from high-resolution Vp and Vs models beneath Mount St. Helens, Washington State, USA. *Geology*, *44*(6), 411–414. https://doi.org/10.1130/G37591.1

Leeman, W. P., Lewis, J. F., Evarts, R. C., Conrey, R. M., & Streck, M. J. (2005). Petrologic constraints on the thermal structure of the Cascades arc. *Journal of Volcanology and Geothermal Research*, *140*(1-3), 67–105. https://doi.org/10.1016/j.jvolgeores.2004.07.016

Lees, J. M., & Crosson, R. S. (1989). Tomographic inversion for three-dimensional velocity structure at Mount St. Helens using earthquake data. *Journal of Geophysical Research*, *94*(B5), 5716–5728. https://doi.org/10.1029/JB094iB05p05716

Lin, F. C., & Ritzwoller, M. H. (2010). Empirically determined finite frequency sensitivity kernels for surface waves. *Geophysical Journal International*, *182*(2), 923–932. https://doi.org/10.1111/j.1365-246X.2010.04643.x

Lin, F.-C., & Ritzwoller, M. H. (2011). Helmholtz surface wave tomography for isotropic and azimuthally anisotropic structure. *Geophysical Journal International*, *186*(3), 1104–1120. https://doi.org/10.1111/j.1365-246x.2011.05070.x

Mann, M. E., Abers, G. A., Crosbie, K. J., Creager, K. C., Ulberg, C., Moran, S., & Rondenay, S. (2019). Imaging subduction beneath Mount St. Helens: Implications for slab dehydration and magma transport. *Geophysical Research Letters*, *46*, 3163–3171. https://doi.org/10.1029/2018GL081471

McCrory, P. A., Blair, J. L., Waldhauser, F., & Oppenheimer, D. H. (2012). Juan de Fuca slab geometry and its relation to Wadati-Benioff zone seismicity. *Journal of Geophysical Research*, *117*, B09306. https://doi.org/10.1029/2012JB009407

Menke, W. (1989). *Geophysical data analysis: Discrete inverse theory*. New York: Academic.

Moran, S. C., Lees, J. M., & Malone, S. D. (1999). P wave crustal velocity structure in the greater Mount Rainier area from local earthquake tomography. *Journal of Geophysical Research*, *104*(B5), 10,775–10,786. https://doi.org/10.1029/1999JB900036

Obrebski, M., Abers, G. A., & Foster, A. (2015). Magmatic arc structure around Mount Rainier, WA, from the joint inversion of receiver functions and surface wave dispersion. *Geochemistry, Geophysics, Geosystems*, *16*, 178–194. https://doi.org/10.1002/2014GC005581

Parsons, T., Trehu, A. M., Luetgert, J. H., Miller, K. C., Kilbride, F., Wells, R. E., et al. (1998). A new view into the Cascadia subduction zone and volcanic arc: Implications for earthquake hazards along the Washington margin. *Geology*, *26*(3), 199–202. https://doi.org/10.1130/0091-7613(1998)026<0199:ANVITC>2.3.CO;2

Phillips, B. A., Kerr, A. C., Mullen, E. K., & Weis, D. (2017). Oceanic mafic magmatism in the Siletz terrane, NW North America: Fragments of an Eocene oceanic plateau? *Lithos*, *274*, 291–303.

Pollack, H. N., Hurter, S. J., & Johnson, J. R. (1993). Heat flow from the Earth's interior: Analysis of the global data set. *Reviews of Geophysics*, *31*(3), 267–280. https://doi.org/10.1029/93RG01249

Porritt, R. W., Allen, R. M., Boyarko, D. C., & Brudzinski, M. R. (2011). Investigation of Cascadia segmentation with ambient noise tomography. *Earth and Planetary Science Letters*, *309*(1-2), 67–76. https://doi.org/10.1016/j.epsl.2011.06.026

Reed, J. C., Wheeler, J.O. & Tucholke, B.E., Compilers, (2004). Geologic map of North America: Decade of North American *Geology Continental Scale Map 001*, Boulder, Geological Society of America, scale 1:5,000,000.

Rees Jones, D. W., Katz, R. F., Tian, M., & Rudge, J. F. (2018). Thermal impact of magmatism in subduction zones. *Earth and Planetary Science Letters*, *481*, 73–79. https://doi.org/10.1016/j.epsl.2017.10.015

Reynard, B. (2013). Serpentine in active subduction zones. *Lithos*, *178*, 171–185. https://doi.org/10.1016/j.lithos.2012.10.012

Schmandt, B., & Humphreys, E. (2011). Seismically imaged relict slab from the 55 Ma Siletzia accretion to the northwest United States. *Geology*, *39*(2), 175–178. https://doi.org/10.1130/G31558.1

Schuster, J. Eric. *Geologic map of Washington State*, Geologic Map GM-53, Washington State Department of Natural Resources, 2005.

Shapiro, N. M., & Campillo, M. (2004). Emergence of broadband Rayleigh waves from correlations of the ambient seismic noise. *Geophysical Research Letters*, *31*, L07614. https://doi.org/10.1029/2004GL019491

Shen, W., & Ritzwoller, M. H. (2016). Crustal and uppermost mantle structure beneath the United States. *Journal of Geophysical Research: Solid Earth*, *121*, 4306–4342. https://doi.org/10.1002/2016JB012887

Sisson, T. W., Salters, V. J. M., & Larson, P. B. (2014). Petrogenesis of Mount Rainier andesite: Magma flux and geologic controls on the contrasting differentiation styles at stratovolcanoes of the southern Washington Cascades. *Bulletin of the Geological Society of America*, *126*(1–2), 122–144. https://doi.org/10.1130/B30852.1

Stanley, W. D., Finn, C., & Plesha, J. L. (1987). Tectonics and conductivity structures in the Southern Washington Cascades. *Journal of Geophysical Research*, *92*(B10), 10,179–10,193. https://doi.org/10.1029/JB092iB10p10179

Stanley, W. D., Johnson, S. Y., Qamar, A. I., Weaver, C. S., & Williams, J. M. (1996). Tectonics and seismicity of the southern Washington Cascade range. *Bulletin of the Seismological Society of America*, *86*, 1–18.

Syracuse, E. M., & Abers, G. A. (2006). Global compilation of variations in slab depth beneath arc volcanoes and implications. *Geochemistry, Geophysics, Geosystems*, *7*, Q05017. https://doi.org/10.1029/2005GC001045

Syracuse, E. M., van Keken, P. E., & Abers, G. A. (2010). The global range of subduction zone thermal models. *Physics of the Earth and Planetary Interiors*, *183*(1–2), 73–90. https://doi.org/10.1016/j.pepi.2010.02.004

Till, C. B., Kent, A. J. R., Abers, G. A., Janiszewski, H. A., Gaherty, J. B., & Pitcher, B. W. (2019). The causes of spatiotemporal variations in erupted fluxes and compositions along a volcanic arc. *Nature Communications*, *10*(1), 1350. https://doi.org/10.1038/s41467-019-09113-0

Ulberg, C., Creager, K., Moran S., Abers, G., Crosbie, K., Crosson, R. et al. (2017), Imaging seismic zones and magma beneath Mount St. Helens with the iMUSH broadband array, *abstr. V11C-0367, Amer. Geophys. Un. 2017 Fall Meeting,* New Orleans LA, 11-15 Dec.

Valley, P. M., Whitney, D. L., Paterson, S. R., Miller, R. B., & Alsleben, H. (2003). Metamorphism of the deepest exposed arc rocks in the Cretaceous to Paleogene Cascades belt, Washington: Evidence for large-scale vertical motion in a continental arc. *Journal of Metamorphic Geology*, *21*(2), 203–220. https://doi.org/10.1046/j.1525-1314.2003.00437.x

van Keken, P. E., Wada, I., Abers, G. A., Hacker, B. R., & Wang, K. (2018). Mafic high-pressure rocks are preferentially exhumed from warm subduction settings. *Geochemistry, Geophysics, Geosystems*, *19*(9), 2934–2961. https://doi.org/10.1029/2018GC007624

Wada, I., & Wang, K. (2009). Common depth of slab-mantle decoupling: Reconciling diversity and uniformity of subduction zones. *Geochemistry, Geophysics, Geosystems*, *10*, Q10009. https://doi.org/10.1029/2009GC002570

Waite, G. P., & Moran, S. C. (2009). VP Structure of Mount St. Helens, Washington, USA, imaged with local earthquake tomography. *Journal of Volcanology and Geothermal Research*, *182*(1–2), 113–122. https://doi.org/10.1016/j.jvolgeores.2009.02.009

Wang, Y., Lin, F. C., Schmandt, B., & Farrell, J. (2017). Ambient noise tomography across Mount St. Helens using a dense seismic array. *Journal of Geophysical Research: Solid Earth*, *122*, 4492–4508.

Weaver, C. S., & Smith, S. W. (1983). Regional tectonic and earthquake hazard implications of a crustal fault zone in southwestern Washington. *Journal of Geophysical Research*, *88*(B12), 10,371–10,383. https://doi.org/10.1029/JB088iB12p10371

Wells, R., Bukry, D., Friedman, R., Pyle, D., Duncan, R., Haeussler, P., & Wooden, J. (2014). Geologic history of Siletzia, a large igneous province in the Oregon and Washington Coast Range: Correlation to the geomagnetic polarity time scale and implications for a long-lived Yellowstone hotspot. *Geosphere*, *10*(4), 692–719. https://doi.org/10.1130/GES01018.1

Wessel, P., & Smith, W. H. F. (1991). Free software helps map and display data. *Eos, Transactions American Geophysical Union*, *72*(41), 441. https://doi.org/10.1029/90EO00319

Yao, H., van Der Hilst, R. D., & De Hoop, M. V. (2006). Surface-wave array tomography in SE Tibet from ambient seismic noise and two-station analysis—I. Phase velocity maps. *Geophysical Journal International*, *166*(2), 732–744. https://doi.org/10.1111/j.1365-246X.2006.03028.x

Yao, Z., & Roberts, R. (1999). A practical regularization for seismic tomography. *Geophysical Journal International*, *138*(2), 293–299. https://doi.org/10.1046/j.1365-246X.1999.00849.x